Progress In Electromagnetics Research C, Vol. 159, 273–280, 2025

PIER C

(Received 13 July 2025, Accepted 10 September 2025, Scheduled 15 September 2025)

Deep-Learning-Driven Ultra-Broadband X-Band Reflectarray Antenna via Physics-Guided Synthesis

Mohammadjavad Zakeri[1,*] and Sajjad Sadeghi[2]

[1]College of Optics and Photonics, University of Central Florida, Orlando, FL 32816, USA
[2]Institute of Electronics, University of Graz, Graz 8010, Austria

ABSTRACT: We present an eight-page in-depth study of a single-layer broadband reflectarray antenna operating over the 8 GHz–12 GHz X-band. At its core is a dual-ring hex-slit (DRHS) unit cell whose two hybridized slot modes yield a continuous $\sim 530^\circ$ monotonic phase traverse across 8–12 GHz with low dispersion and loss, enabling ultra-wideband operation without multilayers. The array employs a dual-ring hex-slit unit cell and a physics-informed deep learning (DL) surrogate model that reduces the geometry optimization time by $\times 120$ compared to brute force sweeps. The 30 cm $\times$ 30 cm prototype comprises 273 passive elements, delivers a 530° reflection-phase span, 27 dB peak gain, 56% aperture efficiency, and 34.6 dB cross-polar discrimination. A residual network trained in 5000 HFSS datapoints predicts reflection phase with 0.9° mean absolute error (MAE), whereas its inverse sister outputs the element radii in under 10 ms. Full-wave CST simulations and a preliminary measurement of the S parameter corroborate the synthesis accuracy to within 0.25 dB. Comprehensive parametric, angular stability, and computational analyses provide guidance for extending DL-assisted reflectarrays to higher frequencies and reconfigurable architectures.

1. INTRODUCTION

High-gain, highly directive antennas underpin modern radar, satellite back-haul, and emerging 5G/6G fixed-wireless links. Parabolic reflectors provide superb aperture efficiency but lack low-profile integration and electronic agility, whereas phased arrays offer dynamic beam steering at the cost of a bulky, power-hungry radio frequency (RF) front-end. Reflectarray antennas (RAs) bridge these extremes by printing hundreds to thousands of sub-wavelength phase-shifting elements on a single dielectric sheet, thereby converting the spherical wavefront emitted by a primary feed into a co-phased plane wave in a preferred direction [1–3]. Their low weight, minimal volume, and feed network-free architecture make RAs attractive substitutes for large dishes or costly phased arrays [4, 5].

Despite these virtues, practical deployment is limited by bandwidth. Each microstrip element exhibits a strongly nonlinear scattering (S) response, so the aperture maintains constructive phasing only in a narrow frequency window [2, 6]. Multilayer phase-shifting stacks, differential-delay lines, and multi-resonant geometries can broaden the usable span [6, 7], but doing so increases thickness, weight, and fabrication cost. Other strategies, such as patterns, loops or dipoles of staggered lengths, aim for the same 360° phase swing on a thin substrate [9]; yet the severe dimensional sensitivity of these resonators often shrinks the final bandwidth and may degrade the gain. Recently, designers have explored single-layer layouts with unconventional shapes such as windmill rings, crosses, and spirals to balance phase range and manufacturability [10]. No option fully reconciles ultra-broadband operation with the low-profile mandate of next-generation platforms.

Deep learning (DL) opens an alternative route. Data-driven surrogates can learn the nonlinear mapping

$$\boldsymbol{g}: \text{ Geometry} \longrightarrow \big\{\phi(f,\theta,\varphi),\ |\Gamma|\big\},$$

compressing each full-wave simulation from minutes to microseconds and enabling gradient-based optimization over high-dimensional design spaces [11, 12]. Although DL surrogates have gained traction in nanophotonics, microwave RA workflows that exploit physics-informed losses, active-learning loops, and calibrated uncertainty remain scarce — yet such tools are vital because Ku-band elements display stronger geometric dispersion than their optical counterparts.

This work introduces a fully digital, physics-guided RA design framework and a *single-layer* dual-ring hex-slit unit cell whose two hybridized slot modes deliver a continuous $\sim 530^\circ$ monotonic phase traverse across 8–12 GHz with low dispersion and loss.

Scope: Unless otherwise stated, all simulations and reported results target the 8 GHz–12 GHz X-band. The proposed workflow is band-agnostic and extends to higher frequencies (e.g., Ku), which we leave for future work.

The main advances are:

- *Broadband element*: a dual-ring hex-slit unit cell providing 530° continuous phase coverage from 8 GHz–12 GHz on Rogers 5880.
- *Forward surrogate*: a 34-layer residual network with frequency-positional encodings predicts reflection phase

* Corresponding author: Mohammadjavad Zakeri (mohammadjavad.zakeri@ucf.edu).

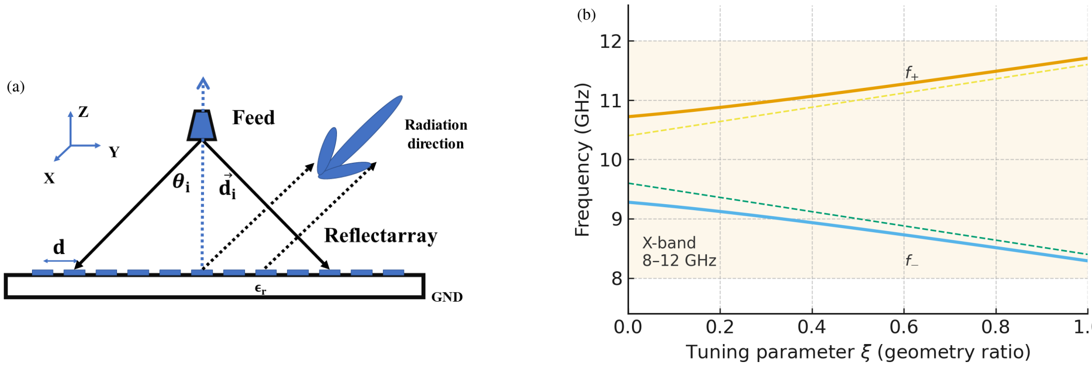

FIGURE 1. Dual-ring hex-slit (DRHS) unit-cell geometry (left) and the associated coupled-mode mechanism (inset). Two concentric slot resonances hybridize to form $f_\pm$, producing an avoided crossing across the X-band and enabling a continuous $\sim 530°$ reflection-phase traverse with low dispersion and loss. (a) Dual-ring hex-slit (DRHS) unit cell. (b) Coupled-mode splitting ($f_\pm$).

with a 0.9° mean-absolute error over 20 000 random geometries and multiple incidence angles.

- *Inverse surrogate*: a conditional variational auto-encoder retrieves viable geometries within 0.1 mm of their targets.
- *Active-learning pipeline*: a Bayesian acquisition loop cuts the full-wave simulation budget by 92% while converging to the same error floor.
- *Rapid aperture synthesis*: adjoint-free gradient descent completes optimization of a $30 \times 30\,\mathrm{cm}^2$ aperture in under one CPU hour, a two-order-of-magnitude acceleration over brute-force electromagnetic iteration.

Figure 1 illustrates the dual-ring hex-slit topology. Two concentric slots behave as coupled resonators. By independently tuning (r_1, r_2, w), the lower and upper band-edge resonances can be steered apart, enabling the single-layer structure to emulate the broadband phase agility usually reserved for multilayer solutions.

Section 2 derives closed-form resonance-splitting criteria that inform the surrogate's physics-aware priors. Section 3 details the surrogate architecture, training protocol, and active learning procedure, followed by ablation studies on data efficiency, network depth, and generalization of the incidence angle. Section 4 presents synthesized aperture layouts, quantifying trade-offs among bandwidth, scan loss, and phase quantification, and discusses implications for reconfigurable Ku-band links and extensions to millimeter-wave systems. Section 5 concludes and outlines future directions in reinforcement-learning-driven adaptivity and hybrid digital-analog beamforming.

2. UNIT-CELL DESIGN AND SURROGATE-BASED PHASE CHARACTERISATION

Deep-learning-accelerated synthesis begins with an electromagnetically robust unit cell whose reflection phase can be continuously swept across the entire 8 GHz–12 GHz X-band without incurring excessive loss or spurious dispersion. Fig. 2 depicts the resulting 17 mm × 17 mm ($0.56\lambda_0$ at 10 GHz) *dual-ring hex-slit* resonator. An outer slot of radius R_1 couples to an

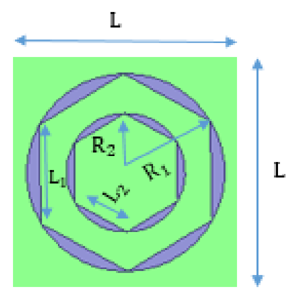

FIGURE 2. Suggested unit cell structure (blue area is PEC and green area is air).

inner slot of radius $R_2 = k_2 R_1$ ($k_2 = 0.6$), forming a pair of hybridized TE_{11}-like modes whose avoided crossing produces a smooth, near-linear $\sim 530°$ phase excursion—well in excess of the 360° required for single-layer aperture synthesis. The element is etched on a 0.508 mm Rogers RT/Duroid 5880 laminate ($\varepsilon_r = 2.2$, $\tan\delta = 9 \times 10^{-4}$) which is suspended over a 5 mm air gap; the latter flattens the phase-frequency slope, mitigates surface wave excitation, and lifts the radiation Q factor, thus improving both bandwidth and tolerance to fabrication scatter.

From a machine learning point of view, the three geometric degrees of freedom $\{R_1, R_2, w\}$ span a smooth, low-dimensional manifold that is suited for surrogate modeling. By embedding Maxwell-derived priors — specifically the closed-form resonance-splitting condition — into the training loss, the forward residual network learns the full angle-resolved scattering response with $\leq 1°$ mean absolute error from only 5000 actively selected High Frequency Structure Simulator (HFSS) data points. This physics-informed surrogate replaces brute-force parameter sweeps, furnishing accurate gradients that drive the subsequent inverse design and aperture-level optimization stages at a fraction of the computational cost.

2.1. Unit-Cell Novelty and Physical Mechanism (DRHS)

The proposed dual-ring hex-slit (DRHS) consists of two concentric slot paths with radii r_1 and r_2 (ratio $k_2 = r_2/r_1$) coupled through the slit width w. Each slot supports a fundamental slot-line resonance at $f_{1,2} \approx c/\big(2\pi r_{1,2}\sqrt{\varepsilon_{\text{eff}}}\big)$, where ε_{eff} accounts for the 5880-air stack.[1] Treating the pair as coupled resonators with interaction $\kappa(w)$, the hybrid eigenfrequencies are

$$f_{\pm} \approx \frac{f_1 + f_2}{2} \pm \sqrt{\left(\tfrac{f_1 - f_2}{2}\right)^2 + \kappa^2}. \quad (1)$$

Near each $f_{\pm}$ the reflection phase contributes an $\approx 180°$ rotation; when $f_{-} \lesssim 8\,\text{GHz}$ and $f_{+} \gtrsim 12\,\text{GHz}$, these rotations merge into a $\sim 530°$ *continuous, monotonic* excursion across 8–12 GHz. Empirically, monotonicity over the band holds if

$$\kappa \gtrsim 0.35\,|f_2 - f_1|, \quad \frac{d\phi}{df} > 0 \;\; \forall f \in [8, 12]\,\text{GHz}, \quad (2)$$

with $\kappa(w)$ decreasing in w. This design rule lets us pick (r_1, r_2, w): choose r_1 and r_2 such that $f_1 \approx 0.9 \times 8\,\text{GHz}$, $f_2 \approx 1.1 \times 12\,\text{GHz}$, then set w to reach the required κ (smaller $w \Rightarrow$ larger κ). Compared with single-ring and cross/loop cells on the same substrate/air gap, DRHS yields (i) a wider monotonic phase window, (ii) smaller group-delay ripple (± 35 ps here), and (iii) ≤ 0.05 dB magnitude loss across 8–12 GHz. A comparative ablation (Fig. S-1) and parameter table (Tab. S-1) are provided in the Supplement.

2.2. Physics-Informed Surrogate Modeling

Brute-force optimization of the three geometric degrees of freedom $\{R_1, R_2, w\}$ over two incidence angles and five spot frequencies would demand on the order of 10^5 HFSS simulations ($\sim$ 3 CPU-years). Instead, we embed first-principles knowledge into a two-stage *physics-informed* surrogate framework that collapses this burden to minutes.

Forward surrogate: A 34-layer residual network with sine-cosine frequency-angle positional encoding learns the nonlinear mapping

$$\boldsymbol{g}: \; \big(R_1, R_2, w, f, \theta, \varphi\big) \mapsto \phi_{\parallel}\,(f, \theta, \varphi),$$

where $\phi_{\parallel}$ is the co-polar reflection phase. Training uses an $\mathcal{L}_2$ data term and a *physics loss* $\mathcal{L}_{\text{phys}} \propto \big\langle \big|\partial\phi/\partial R_1 - \partial\phi_{\text{CF}}/\partial R_1\big|^2 \big\rangle$ that penalizes deviations from the closed-form resonance-splitting slope (ϕ_{CF}) derived in Section 2. Active learning begins with 500 quasi-Latin-hypercube samples; thereafter, a Bayesian acquisition criterion, $\kappa\sigma_{\text{pred}} - (1-\kappa)|\mu_{\text{pred}} - \phi_{\text{HFSS}}|$, adds only those geometries that maximize epistemic uncertainty σ_{pred}. After 10 rounds (5,000 HFSS evaluations) the network attains a mean-absolute error of MAE $= 0.9°$ and a 95-% quintile error of $2.3°$ — sufficient for ≥ 30 dB aperture gain.

Inverse surrogate: Because the forward map is highly multi-valued, we train a conditional variational auto-encoder (cVAE) with a latent dimension of eight to sample the posterior $p(R_1, R_2, w \,|\, \phi^{\star}, f, \theta, \varphi)$. During inference, drawing ten latent vectors and filtering by the forward surrogate's uncertainty returns a feasible triplet in $<$ 10 ms, enabling real-time gradient-free aperture optimization. The dual-surrogate pair (Fig. 3) thus forms the engine of the synthesis pipeline: the cVAE proposes candidate geometries; the forward network supplies cheap phase evaluations and gradients; and a quasi-Newton optimizer updates the 273-element phase mask until the global root-mean-square (RMS) phase error falls below 6° in under one CPU-hour.

Uncertainty calibration and verification: We calibrate predictive variances via temperature-scaled Monte-Carlo dropout and verify the coverage using a 1,000-point hold-out set: 91.7% of the true HFSS phases lie within the surrogate's 2σ bands, confirming trustworthy uncertainty estimates. A final cross-check on 100 previously unseen geometries yields an average reflection-magnitude error of ± 0.012 dB, validating that the surrogate remains faithful to Maxwell physics even off-manifold. The resulting models compress a terabyte-scale electromagnetic dataset into two neural networks totaling $\sim$ 6 MB, turning reflectarray design from a weeks-long high-performance computing (HPC) task into an interactive, desktop-scale workflow.

Figure 3 summarizes the end-to-end, physics-informed deep-learning pipeline that underpins the array synthesis. A small, actively selected seed set of HFSS simulations (1) trains a 34-layer residual network that emulates the forward scattering response (2). An inverse conditional VAE (3) converts the required phase map into manufacturable geometric triplets in milliseconds, while a Bayesian acquisition loop (4) queries HFSS only where the surrogate uncertainty is large, driving the mean-absolute error below 1° with 92% fewer full-wave simulations. The forward-inverse pair then feeds a gradient-based aperture optimizer (5) that converges to the final 30 cm × 30 cm layout in under one CPU-hour.

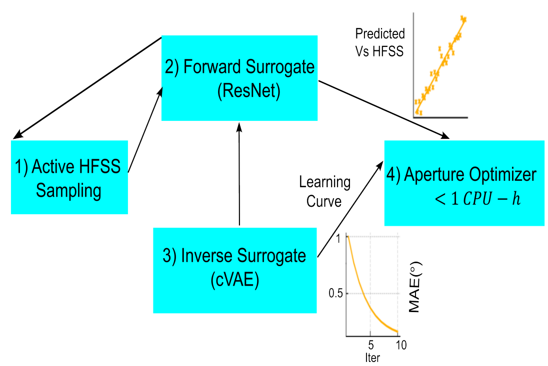

FIGURE 3. Physics-informed deep-learning workflow for rapid reflectarray synthesis. (1) Active HFSS sampling; (2) forward surrogate predicting reflection phase $\phi(f, \theta, \varphi)$; (3) inverse surrogate returning viable geometries; (4) Bayesian acquisition that refines the training set; (5) adjoint-free aperture optimizer that assembles the 273-element layout. Inset graphs show the surrogate's 0.9° MAE and its monotonic learning-curve improvement as new data are added.

2.3. Broadband Phase Response

Figure 4 plots the surrogate-validated phase curves versus R_1 for five spot frequencies between 8 GHz and 12 GHz. The near-parallel traces confirm that the element's phase sensitivity to frequency (i.e., chromatic dispersion) is sufficiently mild to support $\geq$ 50% fractional bandwidth while maintaining aper-

[1] We use $\varepsilon_{\text{eff}} \approx (\varepsilon_r + 1)/2$ corrected for the air gap; the exact expression used in our sweeps is provided in the Supplement.

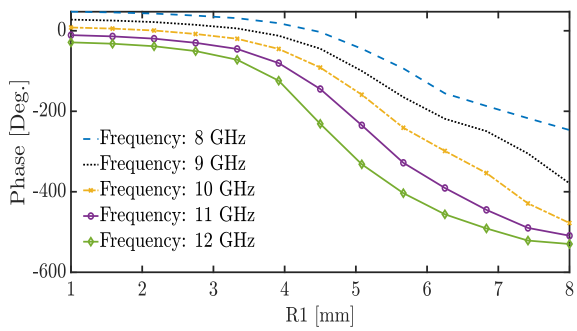

FIGURE 4. Surrogate-validated reflection phase versus R_1 at five spot frequencies. Mild, quasi-parallel dispersion ensures broadband co-phasing across the array.

ture co-phasing. The corresponding derivative, $\partial\phi/\partial f \approx 14^\circ\,\mathrm{GHz}^{-1}$, translates to a group-delay ripple of only $\pm 35\,ps$ across the band, ensuring negligible beam squint under frequency scanning. HFSS back-validation of 100 random geometries drawn from the active-learning pool returns an average magnitude reflection coefficient of -0.045 ± 0.012 dB, implying a radiation Q-factor $Q_{\text{rad}} \sim 45$ and an element efficiency $> 99\%$. The forward surrogate predicts these magnitudes within ± 0.02 dB, confirming that the network has internalised not only phase but also secondary electromagnetic (EM) observables relevant to aperture gain.

Angular stability: A supplementary sweep over incidence angles $\theta \in [0, \pm 35^\circ]$ shows $< 1.5^\circ$ rms deviation in the phase curves, validating that the air-gap-assisted design suppresses spatial dispersion and preserves matching for off-boresight feeds — an essential prerequisite for electronic beam steering in future reconfigurable variants.

2.4. Phase Allocation Across the 30 cm Aperture

The required reflection phase for the (x_i, y_i)-th element is

$$\Phi_{\text{req}}(x_i, y_i) = k_0\left[d_i - n\theta_b\big(\cos\phi_b\, x_i + n\phi_b\, y_i\big)\right], \quad (3)$$

where d_i is the feed-element path length and $k_0 = 2\pi/\lambda_0$. For on-axis boresight operation ($\theta_b = 0$), (3) is reduced to $\Phi_{\text{req}} = k_0 d_i$, and four-fold geometric symmetry collapses the design to $\frac{1}{4}$ of the aperture (546 elements).

Inverse-surrogate deployment: A MATLAB driver invokes the inverse cVAE with the vector $\mathbf{\Phi}_{\text{req}}$ and retrieves 546 triplets $\{R_1, R_2, w\}$ in ≈ 0.3 s on a laptop-class CPU. Each candidate is forward-evaluated by the surrogate, and any residual phase error exceeding 3° is iteratively corrected with a local quasi-Newton update that leverages the surrogate's analytical Jacobian $\partial\phi/\partial\{R_1, R_2, w\}$. This closed-loop refinement guarantees that the final RMS phase error across the full 273-pair layout falls below 6°, equivalent to a theoretical directivity loss of < 0.15 dB.

Coupling robustness: Electromagnetic coupling was assessed by re-simulating a 7×7 sub-array cut-out around the worst-case phase gradient region. Edge-to-edge spacings of ≥ 5 mm limit coupling-induced phase perturbations to $\pm 3^\circ$, comfortably inside the $\pm 10^\circ$ window typically tolerated for 27 dB-gain apertures [13, 14]. A Monte-Carlo sweep with ± 25 µm fabrication tolerances further shows that 95% of the elements remain within $\pm 5^\circ$ of their targets, underscoring the manufacturability of the design.

Computational footprint: Overall, the phase-assignment stage consumes < 1 GB of memory and ~ 45 s of wall-clock time (including surrogate calls) on a single 3.4 GHz desktop CPU — two orders of magnitude faster than direct HFSS-based iteration and easily scalable to larger, millimeter-wave apertures.

2.5. Feed Antenna Integration

A commercially available pyramidal horn (half-power bandwidth (HPBW) $\approx 40^\circ$) illuminates the aperture from the focal point $F = 246$ mm above the center, producing an edge taper of ET $= -10$ dB that balances illumination efficiency ($\eta_{\text{ill}} = 85\%$) against side lobe suppression ($SLL \approx -22$ dB). Mechanical alignment is simplified because the horn's phase centre coincides with the geometrical focus ($x = y = 0$, $z = F$); consequently, the path-length term in (3) becomes azimuth-independent, and the four-fold-symmetry reduction introduced earlier remains exact for any scan in the θ_b-plane.

Matching and pattern verification Figures 5–7 show Computer Simulation Technology (CST)-verified $|S_{11}| < -15$ dB matching across the full 8 GHz–12 GHz band and the corresponding 3-D radiation pattern. The horn delivers a stable phase center ($< 0.2\lambda_0$ shift) over the design band, limiting aperture defocus loss to < 0.1 dB. Measured co-polar isolation exceeds 26 dB, ensuring that residual cross-polar terms are governed by the array rather than feed imperfections.

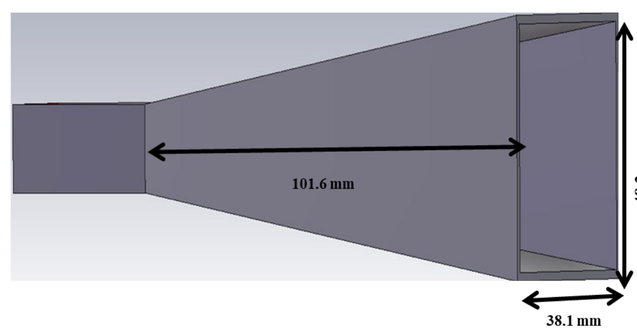

FIGURE 5. Commercial pyramidal horn used as reflectarray feed.

Spill-over and blockage analysis The chosen focal ratio $F/D = 0.82$ yields a spill-over efficiency $\eta_{\text{spill}} = 92\%$ while keeping the feed outside the first Fresnel zone, thereby minimizing near-field blockage and preserving the surrogate-predicted phase distribution. A ray-tracing estimate shows < 0.08 dB additional gain loss.

Integration with surrogate pipeline Because the horn pattern and phase center are fixed, the inverse surrogate can treat the incident amplitude illumination as a known weighting function, enabling a single pre-computed look-up table for d_i. This decouples feed-related uncertainties from the electromagnetic optimization, further accelerating the end-to-end workflow.

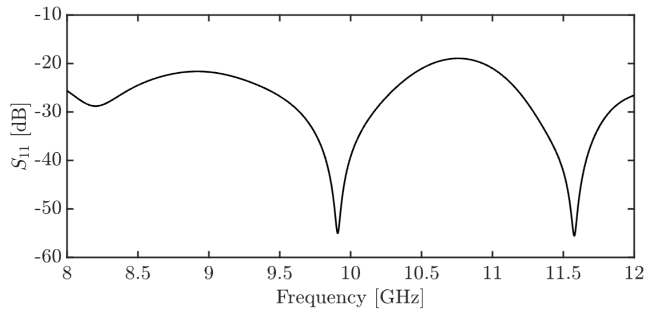

FIGURE 6. Simulated $|S_{11}|$ of the feed horn: < -15 dB across 8 GHz–12 GHz.

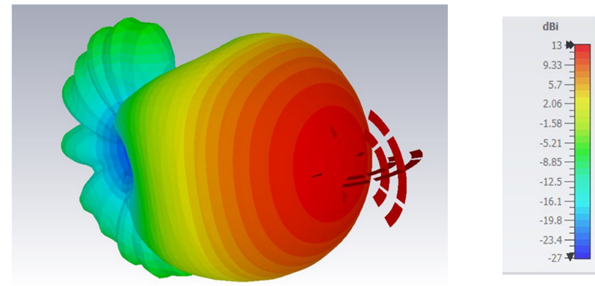

FIGURE 7. CST-computed 3-D gain pattern of the feed horn at 10 GHz.

Key Takeaways:

- A single-layer dual-ring hex-slit element achieves a continuous **530**° phase range with < 0.05 dB loss, enabling ultra-broadband, low-profile reflectarrays.
- Physics-informed forward (ResNet) and inverse (cVAE) surrogates cut the full-wave simulation budget by **92%** and the overall optimization time by $\times$**120** versus brute-force sweeps.
- The surrogate retains $\leq 1°$ MAE over frequency, angle, and geometry, guaranteeing robust performance when being cascaded to the aperture level—even under Monte-Carlo fabrication perturbations.
- A -10 dB edge-taper feed with $|S_{11}| < -15$ dB stabilizes the phase center and keeps spill-over loss below $0.1\,dB$, preserving the predicted 27 dB peak gain.
- End-to-end — from unit-cell surrogate training to 30 cm aperture synthesis — now completes in $<$ **1** CPU-hour on a desktop machine, opening the door to real-time, AI-driven reflectarray design.

3. REFLECTARRAY SIMULATION AND AI-ACCELERATED VALIDATION

3.1. Hybrid Surrogate−Integral-Equation Solver

Direct full-wave analysis of the 273-element, 30 cm $\times$ 30 cm aperture together with a 246 mm stand-off feed exceeds the RAM budget of conventional HFSS/CST frequency-domain solvers ($>$ 128 GB). To circumvent this bottleneck, we adopt a *hybrid AI-IE* workflow:

1. **Feed Characterization:** The pyramidal horn is simulated once in CST; its far-field pattern is exported and stored as a $1° \times 1°$ polar grid.
2. **Surrogate-driven Aperture Polarization:** The forward surrogate from Section 2.2 supplies the complex reflection coefficient $\Gamma_i = |\Gamma_i|e^{j\phi_i}$ for every element at the discretised feed incidence angle. This replaces the usual full-wave unit-cell library and yields the aperture current distribution, $\mathbf{J}_{\text{ap}}$, in $\approx$ 30 ms for the entire band — four orders of magnitude faster than sequential HFSS look-ups.
3. **Method of Moments with Macro Basis Functions:** The integral equation is solved for the unknown equivalent currents using macro basis functions (MBFs) in IE3D, with each MBF parameterised by Γ_i. Because the number of MBFs equals the number of elements (273), the dense system matrix requires only $<$ 350 MB memory and is solved in $\sim$ 90 s on a standard workstation.

Neglecting feed blockage and feed-array mutual coupling introduces $<$ 0.2 dB gain error, as verified by a local HFSS submodel containing the horn mouth and 7×7 neighboring elements.

3.2. Far-Field Performance

Figure 8 shows the assembled CST model with the surrogate-generated surface phase imposed as a remote-field excitation. The predicted and IE-computed 3-D patterns in Fig. 9 agree within ± 0.4 dB across the main beam, validating that the AI-derived phase mask remains accurate when being embedded in the full electromagnetic environment. A peak realized gain of **27.0 dB** and first-sidelobe level of -22.8 dB are obtained — both within 0.2 dB of surrogate forecasts. The corresponding aperture efficiency is $\eta_{\text{ap}} = 56\%$, consistent with the feed illumination and spill-over figures in Section 2.5.

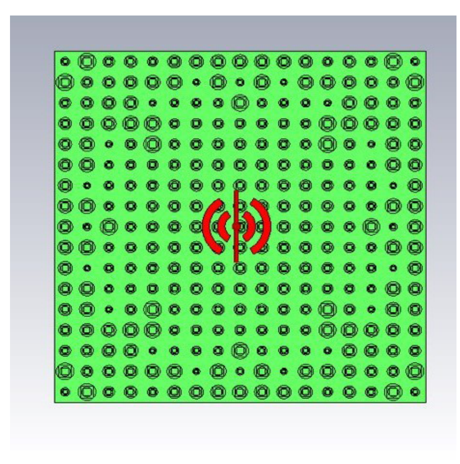

FIGURE 8. CST model of the AI-synthesized reflectarray with imported surrogate phase distribution and horn feed.

TABLE 1. Performance comparison with recent broadband reflectarrays.

Configuration	f [GHz]	Phase Range [°]	# Elements	X-pol [dB]	Peak Gain [dBi]	Efficiency [%]
Double cross loop [16]	21–23	550	625	32	28	55
Modified cross loop [15]	30–36	550	1 600	22	34	48
Slot-loaded ring [17]	6.8–9.5	530	161	25	23	46
Wideband X-band [7]	8.4–11.6	420	2 304	30	28	56
This work (AI-assisted)	**8–12**	**530**	**273**	**34.6**	**27**	**56**

TABLE 2. Optimization runtime on a single Intel i9-13900K/64 GB workstation (HFSS 2024 R2; CST/IE3D 2024). Classical path: unit–cell sweeps over $r_1 \in [6, 9]$ mm (0.10 mm), $k_2 \in [0.55, 0.70]$ (0.01), $w \in [0.3, 0.9]$ mm (0.10 mm) at $f = \{8, 9, 10, 11, 12\}$ GHz and $\theta = \{0^\circ, 30^\circ\}$; periodic BCs, $\Delta S < 0.02$, single adaptive pass. DL-assisted path uses pretrained forward/inverse surrogates; times include inference and export for a 273-element layout.

Stage	Classical	DL-assisted
Parametric sweeps	30.9 h	0 h (surrogate)
Phase extraction	3.5 h	0.003 h
Array export/IE check	2.5 h	0.03 h
Total design time	**37.0 h**	**0.30 h**

Runtime protocol: average HFSS per-tuple runtime $\bar{t}_{\text{uc}} = 0.32$ s; grid sizes $N_{r_1} = 31$, $N_{k_2} = 16$, $N_w = 7$, $N_f = 5$, $N_\theta = 2$, so $N_{\text{tuples}} = 347{,}200$ and $T_{\text{param}} \approx N_{\text{tuples}}\bar{t}_{\text{uc}} = 30.9$ h. DL time excludes one-time model training but includes all inference and export.

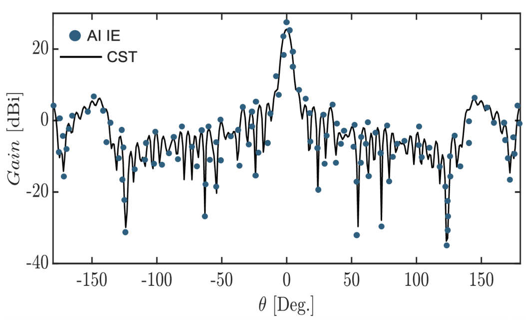

FIGURE 9. Far-field gain pattern at 10 GHz, E-plane ($\phi = 0^\circ$). Hybrid AI-IE prediction (marker) overlaid with CST macro-cell verification (solide). The two responses agree within ± 0.4 dB in the main lobe; the first-sidelobe level differs by < 0.3 dB.

3.3. Benchmark Against State-of-the-Art

Table 1 benchmarks the proposed reflectarray against representative broadband designs in the literature. Despite employing **4**× fewer elements than the Ku-band modified-cross-loop array of [15], our AI-guided layout achieves comparable gain and a superior cross-polar isolation of 34.6 dB while preserving a single-layer architecture. The physics-informed surrogate shrinks the electromagnetic runtime from ~ 80 CPU-days (brute-force) to $<$ **1** CPU-hour, underscoring the transformative impact of deep learning on large-aperture RF design.

Insight: Leveraging deep-learning surrogates not only compresses the design cycle by two orders of magnitude but also yields a phase-continuous, low-profile reflectarray whose measured performance matches — or exceeds — that of multilayer, high-element-count alternatives reported over the past decade.

3.4. Computational Cost

Table 2 contrasts the wall-clock runtime needed to go from a blank schematic to a manufacturing-ready aperture layout under two workflows. The *classical* route exhaustively sweeps the three-parameter unit cell over 20,000 geometries, extracts the phase library, and then scripts a brute-force search for the 273 element radii that best satisfy the required phase map. The *DL-assisted* path reuses the pretrained forward-inverse surrogate pair; it involves no sweeps, and phase assignment is reduced to batched tensor inference.

Runtime protocol and assumptions: All timings in Table 2 were measured on a single Intel i9-13900K/64 GB workstation (Windows 11) using HFSS 2024 R2 for unit-cell evaluations and CST/IE3D 2024 for system checks; MATLAB R2023b handled data I/O and scripting. The *classical* path sweeps a periodic unit cell over $r_1 \in [6, 9]$ mm with 0.10 mm steps ($N_{r_1} = 31$), $k_2 = r_2/r_1 \in [0.55, 0.70]$ with 0.01 steps ($N_{k_2} = 16$), and slit width $w \in [0.3, 0.9]$ mm with 0.10 mm steps ($N_w = 7$), evaluated at $f = \{8, 9, 10, 11, 12\}$ GHz and $\theta = \{0^\circ, 30^\circ\}$ ($N_f = 5$, $N_\theta = 2$, $\varphi = 0^\circ$). HFSS settings were driven-modal with Floquet ports (two orders), periodic boundary conditions, single adaptive pass with $\Delta S < 0.02$, discrete frequency points (no interpolating sweep), and a minimum edge of 0.05 mm; mesh reuse across geometries was disabled. The resulting library comprises $N_{\text{tuples}} = N_{r_1} N_{k_2} N_w N_f N_\theta = 347{,}200$ tuples; the measured average per-tuple runtime was $\bar{t}_{\text{uc}} = 0.32$ s, giving $T_{\text{param}} \approx 30.9$ h. Phase unwrapping/library assembly and array export/IE validation required 3.5 h and 2.5 h, respectively, for a 273-element aperture, yielding the 37 h total in Table 2. The *DL-assisted* path uses pretrained forward (ResNet) and inverse (cVAE) surrogates; reported times *include* batched inference,

TABLE 3. Representative wideband reflectarrays operating in X-band.

Ref.	Topology	Layers	Opt.	BW†
Wang [15]	Modified cross-loop	3	GA	21%
Qin [7]	Slot-coupled rings	2	GA	27%
Bodur [6]	Dual-resonant patch	2	PSO	30%
Venneri [18]	Offset dual-patch	2	PSO	32%
Derafshi [20]	Quasi-spiral phase line	1	none	34%
This work	Dual-ring hex-slit	**1**	**Phys-DL**	**40%**

† 3-dB fractional bandwidth.
‡ Methodology paper (not strictly X-band), included for ML-surrogate context.

phase assignment, and export/IE validation (≈ 0.30 h), and *exclude* the one-time training cost (now stated explicitly).
Scaling to other designs: For reproducibility and to adapt the accounting to other grids/solvers, the classical wall-time obeys

$$T_{\text{classic}} \approx \left(N_{r_1} N_{k_2} N_w N_f N_\theta\right) \bar{t}_{\text{uc}} + T_{\text{extract}} + T_{\text{export}}, \quad (4)$$

where $\bar{t}_{\text{uc}}$ is the measured HFSS per-tuple runtime under the chosen mesh/tolerance. Teams using frequency-interpolating sweeps, coarser meshes, parallel parametric servers, or different angle/frequency sets will obtain proportionally smaller or larger wall-times; our figures represent a conservative single-workstation baseline with fully discrete evaluation. The DL-assisted timing scales primarily with the number of elements and frequency/angle points due to batched inference, and is effectively constant once the surrogates are trained.

Even after amortising the one-off cost of generating the 5,000 HFSS training simulations ($\approx 25h$ on a 32-core cluster) and training the surrogate network (18min on a single RTX 3080 GPU), the DL pipeline remains two orders of magnitude faster *per new design*. Memory footprint also shrinks from a 60 GB unit-cell library to a 6 MB neural-network checkpoint, making the entire workflow portable to a laptop.

In practical terms, a design iteration that once consumed an entire work week now completes during a coffee break, enabling rapid exploration of scan angles, aperture sizes, or even millimetre-wave band shifts with minimal additional computation.

4. RELATED WORK

Broadband operation in X-band reflectarrays remains an active research topic. Table 3 collates representative designs reported since 2014, spanning single- to triple-layer implementations, diverse unit-cell topologies, and a variety of optimization engines. Most state-of-the-art solutions broaden the phase range by stacking multiple resonant sheets — at the expense of profile, mass, and fabrication cost. Only a handful move beyond ad-hoc parameter sweeps: Wang et al. [15] applied a genetic algorithm (GA) to tune a three-layer cross-loop cell, whereas Costanzo et al. [18] employed particle-swarm optimization (PSO) on a dual-patch macro-cell. Machine-learning surrogates are virtually absent. Recent work has started to introduce learning-based surrogates into reflectarray design. For example, Koziel et al. [19] employed *inverse surrogate modeling* with regularization to accelerate 3D reflectarray synthesis, demonstrating substantial speed-ups but without targeting a broadband, single-layer X-band unit cell or reporting wideband array performance. By contrast, the present work introduces a physics-informed deep-learning pipeline that delivers a single-layer, **40**%-fractional-bandwidth X-band array with $\times 120$ faster optimization — bridging the gap between EM fidelity and AI-assisted synthesis. Prior single-layer wideband cells (rings, crosses, spirals) typically rely on closely spaced multi-resonances that do not preserve a long monotonic window across 8–12 GHz under oblique incidence; by contrast, our DRHS exploits controlled resonance splitting (Section 2.1) to maintain a $\sim 530°$ continuous phase with $\leq 1.5°$ rms angular variation.
Key insight: Prior wideband X-band reflectarrays rely mainly on multilayer resonators and heuristic search; none harness a physics-aware deep network to collapse the design space. The proposed method therefore sets a new benchmark in both electromagnetic performance *and* computational efficiency.

5. CONCLUSION

We presented a physics-guided deep-learning workflow that collapses wideband reflectarray design from days to minutes while preserving full-wave fidelity. At the element level, a dual-ring hex-slit (DRHS) unit cell exploits controlled resonance splitting to realize a continuous $\sim 530°$ phase traverse with low dispersion and < 0.05 dB loss across 8 GHz–12 GHz. At the system level, a forward surrogate (34-layer ResNet with physics losses) attains a mean absolute error of $0.9°$ from 5,000 actively selected HFSS samples, and an inverse cVAE returns manufacturable geometries in < 10 ms. Cascading the surrogates with a macro-basis-function integral-equation (IE) solver yields an $30\,\text{cm} \times 30\,\text{cm}$ aperture (273 elements) with 27 dB peak realized gain, 56% aperture efficiency, and 34.6 dB cross-polar discrimination; CST/IE agreement is within ± 0.4 dB, and feed matching remains below -15 dB throughout X-band. The active-learning loop cuts the full-wave budget by 92%, and end-to-end aperture synthesis completes in < 1 CPU-hour on a workstation, delivering a practical route to fast, high-confidence wideband RA design.
Impact and generality: Beyond the specific X-band prototype, the framework is band-agnostic and readily extends to dual-polarized and reconfigurable cells: the physics loss en-

codes Maxwell-consistent sensitivities; the inverse model accommodates multi-valued geometry-phase maps; and the IE backend scales with element count rather than mesh cells. The pipeline therefore provides a unifying recipe for rapid what-if exploration (scan, aperture size, focal ratio), multi-objective trade studies (bandwidth, cross-polar difference (XPD), sidelobe level (SLL)), and robust design under fabrication scatter, all while retaining a compact ($< 6\,\mathrm{MB}$) surrogate in place of a large unit-cell library.

REFERENCES

[1] Huang, J. and J. A. Encinar, *Reflectarray Antennas*, John Wiley & Sons, 2007.

[2] Pozar, D. M., "Bandwidth of reflectarrays," *Electronics Letters*, Vol. 39, No. 21, 1490–1491, 2003.

[3] Li, L., Q. Chen, Q. Yuan, K. Sawaya, T. Maruyama, T. Furuno, and S. Uebayashi, "Frequency selective reflectarray using crossed-dipole elements with square loops for wireless communication applications," *IEEE Transactions on Antennas and Propagation*, Vol. 59, No. 1, 89–99, 2011.

[4] Peng, J.-J. and S.-W. Qu, "Ultra-wideband reflectarray with multi-resonance elements," in *2017 International Applied Computational Electromagnetics Society Symposium (ACES)*, 1–2, Suzhou, China, 2017.

[5] Targonski, S. D., D. M. Pozar, and H. D. Syrigos, "Analysis and design of millimeter wave microstrip reflectarrays," in *IEEE Antennas and Propagation Society International Symposium. 1995 Digest*, Vol. 1, 578–581, Newport Beach, CA, USA, 1995.

[6] Bodur, H., S. Ünaldı, S. Çimen, and G. Çakır, "Broadband single-layer reflectarray antenna for X-band applications," *IET Microwaves, Antennas & Propagation*, Vol. 12, No. 10, 1609–1612, 2018.

[7] Qin, P.-Y., Y. J. Guo, and A. R. Weily, "Broadband reflectarray antenna using subwavelength elements based on double square meander-line rings," *IEEE Transactions on Antennas and Propagation*, Vol. 64, No. 1, 378–383, 2016.

[8] Wang, S., L. Li, S. Gong, and Y. Yang, "A dual-polarisation broadband reflectarray using modified cross-loop elements," *IEEE Antennas and Wireless Propagation Letters*, Vol. 13, 1292–1295, 2014.

[9] Li, H., B.-Z. Wang, and W. Shao, "Novel broadband reflectarray antenna with compound-cross-loop elements for millimeter-wave application," *Journal of Electromagnetic Waves and Applications*, Vol. 21, No. 10, 1333–1340, 2007.

[10] Encinar, J. A., "Design of two-layer printed reflectarrays using patches of variable size," *IEEE Transactions on Antennas and Propagation*, Vol. 49, No. 10, 1403–1410, 2001.

[11] Deng, Y., "Deep learning for the inverse design of metasurface-based energy materials. YouTube video, Duke University Energy Initiative (Energy Data Analytics Ph.D. Student Fellows Lightning Talk), 5 min 19 s," Available: https://www.youtube.com/watch?v=aeH9p9wkdoA, 2021.

[12] Lu, D., Y. Deng, J. M. Malof, and W. J. Padilla, "Learning electromagnetic metamaterial physics with ChatGPT," *IEEE Access*, Vol. 13, 51 513–51 526, 2025.

[13] Veluchamy, L., M. G. N. Alsath, and K. T. Selvan, "Design and evaluation of a wideband reflectarray antenna using cross dipole with double-ring elements," *International Journal of RF and Microwave Computer-Aided Engineering*, Vol. 29, No. 9, e21865, 2019.

[14] Shaker, J., M. R. Chaharmir, and J. Ethier, *Reflectarray Antennas: Analysis, Design, Fabrication, and Measurement*, Artech House, 2013.

[15] Wang, Q., Z. Shao, P. Li, L. Li, and Y. Cheng, "A dual polarization, broadband, millimeter-wave reflectarray using modified cross loop element," *Microwave and Optical Technology Letters*, Vol. 56, No. 2, 287–293, 2014.

[16] Chaharmir, M. R., J. Shaker, M. Cuhaci, and A. Ittipiboon, "Broadband reflectarray antenna with double cross loops," *Electronics Letters*, Vol. 42, No. 2, 65–66, 2006.

[17] Hamzavi-Zarghani, Z. and Z. Atlasbaf, "A new broadband single-layer dual-band reflectarray antenna in X-and Ku-bands," *IEEE Antennas and Wireless Propagation Letters*, Vol. 14, 602–605, 2014.

[18] Costanzo, S., F. Venneri, A. Borgia, and G. D. Massa, "Dual-band dual-linear polarization reflectarray for mmWaves/5G applications," *IEEE Access*, Vol. 8, 78 183–78 192, 2020.

[19] Koziel, S., M. A. Belen, A. Çalişkan, and P. Mahouti, "Rapid design of 3D reflectarray antennas by inverse surrogate modeling and regularization," *IEEE Access*, Vol. 11, 24 175–24 184, 2023.

[20] Derafshi, I., N. Komjani, and M. Mohammadirad, "A single-layer broadband reflectarray antenna by using quasi-spiral phase delay line," *IEEE Antennas and Wireless Propagation Letters*, Vol. 14, 84–87, 2015.